Environmental Science Advances

ROYAL SOCIETY OF CHEMISTRY

PAPER

View Article Online
View Journal | View Issue

Cite this: *Environ. Sci.: Adv.*, 2023, **2**, 325

Improved photocatalytic activity of ZnO-[10%]BiOI and ZnO-[10%]WO_3 heterostructure in the destruction of 2-chlorobiphenyl†

Darlington C. Ashiegbu, *[a] Nosipho Moloto [b] and Herman Potgieter [ac]

A series of photocatalysts and heterojunction composites comprising ZnO, WO_3, and BiOI with different loadings of WO_3 and BiOI into ZnO was synthesized and applied for the destruction of 2-chlorobiphenyl (2CBP). The surface morphologies and elemental analysis of the as-synthesized composites were determined using a Carl Zeiss Sigma FE-SEM equipped with an Oxford X-act EDS; optical studies were conducted using a UV 1800 Shimadzu UV-vis spectrophotometer. The X-ray diffraction measurements were made with a Bruker D2 XRD instrument, while the BET surface area measurements, BJH pore size distribution, and isotherms were obtained using a Micrometrics TriStar 3000 instrument. The ZnO-[10%]BiOI heterostructure exhibited a superior photocatalytic activity in this study. The degradation reactions were fitted to the pseudo-first and second order kinetic models in order to exploit the kinetic process of the photodegradation reaction. The ZnO-[10%]BiOI hetero-photocatalyst showed the highest rate constants of 0.0054 min^{-1} and 0.0086 min^{-1} in both the first and second order kinetic models, respectively. When compared to undoped ZnO, the rate constant of the ZnO-[10%]BiOI heterostructure was observed to be nearly 5-fold higher, demonstrating the superior catalytic performance of the as-prepared ZnO-[10%]BiOI hetero-structured photocatalyst. All the photocatalysts and heterostructures showed increased rate constants in the second-order reaction kinetics model except for BiOI and ZnO-[5%]WO_3, whose rate constants decreased from 0.0046 to 0.0041 min^{-1} and 0.0036 to 0.0029 min^{-1}, respectively. The kinetic data show that it requires 128.4 min for the measured 2CBP concentration to be halved to the initial concentration when ZnO-[10%]BiOI is applied. A charge separation degradation mechanism is proposed to describe the process. The findings from this study suggest that ZnO-[10%]BiOI can potentially be used as an efficient and effective catalyst for the degradation of recalcitrant organic pollutants in water.

Received 14th September 2022
Accepted 23rd December 2022

DOI: 10.1039/d2va00222a

rsc.li/esadvances

Environmental significance

Polychlorinated biphenyls (PCBs) are synthetic compounds that have been detected in nearly every part of the global environment as pollutants, including water, sediments, air, fish and animals, and human adipose tissue, milk, and serum. PCBs are among the class of pollutants listed as persistent organic pollutants (POPs), together with the 209 PCB congeners. Originally, PCBs were abated by biodegradation, physical processes (such as incineration, solvent extraction, adsorption) and chemical processes (such as the use of nanoscale zero-valent iron *via* dechlorination). However, these processes have proven to be expensive, ineffective, and inefficient and often lead to the production of even more toxic compounds. Photocatalysis has been proposed for the treatment of PCBs, which could be a better alternative to other methods with respect to the United Nations Sustainable Development Goal 6. This study addresses the synthesis of efficient photocatalysts and their subsequent application in the photodestruction of 2CBP. This study also models the reaction kinetics of the photodestruction process in addition to proposing a photodestruction mechanism for the as-synthesized heterostructure.

1. Introduction

Over the past years, research into renewable and sustainable energy has intensified. This is because of the decreasing supplies of fossil fuels and environmental problems caused by their exploitation.[1] Humans and all life forms throughout the world are severely affected as a result of the consumption of impure water and presence of organic, inorganic, and microbial contaminants in water.[2] Consequently, the remediation/clean-

[a]*School of Chemical and Metallurgical Engineering, University of the Witwatersrand Johannesburg, Private Bag X3 PO Wits 2050, Johannesburg, South Africa. E-mail: darlingtonashiegbu1985@yahoo.com; 1580874@students.wits.ac.za*

[b]*School of Chemistry, University of the Witwatersrand Johannesburg, Private Bag X3 PO Wits 2050, Johannesburg, South Africa*

[c]*Department of Natural Science, Manchester Metropolitan University, Chester Street M1 5GD, Manchester, UK*

† Electronic supplementary information (ESI) available. See DOI: https://doi.org/10.1039/d2va00222a

up of organic pollutants has become increasingly necessary. However, the process is expensive, costing nations and corporations a lot of money. The current practices in organic pollutant remediation (ozonation, reverse osmosis, filtration, adsorption, biological treatment, coagulation, incineration) have been reported to be inadequate and are mostly effective when two or more processes are combined.[3] Incineration can result in the emission of toxic volatile gases, while physical methods (adsorption, filtration, reverse osmosis, coagulation) have been reported to be expensive and may not totally eliminate organic pollutants but may transform them to harmful intermediates.[4,5] A long treatment time is required in biological treatment processes coupled with the presence of toxic and recalcitrant pollutants immune to the aforementioned methods, which may also cause unpleasant odors. Ozonation, although effective in some cases, has been reported to be unstable and is also affected by temperature, pH, and salts.[3] In light of these issues, a pressing demand exists for the advancement and implementation of novel advanced treatment technologies for organic pollutant abatement in water and wastewater resources.[6]

Advanced oxidation processes (AOPs) have received a lot of research attention in the last three decades and are now used in organic pollutant abatement because they are cheaper (when compared with other processes), efficient, and environmentally friendly. AOPs are capable of the *in situ* production of hydroxyl radicals ($^{\bullet}OH$), superoxide anion ($^{\bullet}O_2^-$), and electron/hole (e^-/h^+) pairs for the remediation of organic pollutants into CO_2, H_2O, and less harmful products.[6,7] Among the various AOPs (Fenton Processes, UV/H_2O_2, O_3/H_2O_2/UV, O_3/UV, semiconductor photocatalysis), photocatalysis has been reported as the most novel, promising, and "green" alternative. Semiconductor photocatalysts and their development provide potential solutions for pollution remediation in addition to the global energy problem due to the abundance of solar energy.[8]

A variety of semiconductor photocatalysts (TiO_2, ZnO, Fe_2O_3, CdS, and ZnS) have been deployed for the purpose of photooxidation of pollutants with TiO_2 remaining the most studied and utilized material to date.[9–15] This is because of its high oxidative power, economy, photostability, non-toxicity, chemical stability, and quick electron transfer to molecular oxygen under UV light.[16–18] Despite all of the listed positives, TiO_2 has been reported to suffer from major drawbacks, such as difficulty in recovering and utilization of fine titania powders (which has prevented its large scale utilization in photocatalytic processes), higher cost (compared with ZnO), high charge carrier recombination, and low absorption rate over the UV spectrum, among others.[19–22] Due to their near identical bandgap, availability, similar degradation mechanism, large free-exciton binding energy (which ensures prolonged exciton emission even above room temperature), and low cost, ZnO has been identified as a promising candidate capable of competing with TiO_2 because of the exhibition of better absorption efficiency over a larger percentage of the solar spectrum.[23] In addition, several researchers suggested a higher efficiency of ZnO over TiO_2 in the generation of photoactive species, easy fabrication *via* crystal growth anchored on a variety of supports using low temperature, higher electron mobility (about two-folds higher than TiO_2), and higher quantum efficiency (in numerous studies).[24–26]

ZnO is an n-type semiconductor that has been researched for its low cost, easy fabrication *via* crystal growth anchored on a variety of supports using low temperature, high redox potential, high quantum efficiency, and non-toxicity. Regrettably, the practical application of ZnO is restricted by its wide band gap (~3.3 eV), which is linked to its absorption only in the UV spectrum, high carrier recombination, vulnerability to dissolution at acidic pH, low quantum efficiency and photo-corrosion over prolonged illumination (in aqueous solutions).[27,28] Various strategies for the modification of the ZnO semiconductor to improve its photocatalytic activity have been proposed, and currently being extensively studied by researchers. Some of these strategies include the narrowing of the wide bandgap through incorporation of metal or non-metal dopants, integration with other semiconductors with smaller bandgaps, construction of heterojunctions between two or more semiconductors, hydrogenation (annealing in hydrogen environment), and anchoring on carbon nanostructures.[29–31]

Bismuth-based metal oxides (*e.g.*, $Bi_4Ti_3O_{12}$, Bi_2O_3, $BiFeO_3$, $BiFeWO_6$, $BiVO_4$, Bi_2WO_6, Bi_2MoO_6), oxyhalides (BiOI, BiOBr, BiOCl, and BiOF) and sulfides (Bi_2S_3) have recently attracted much interest among materials scientists, and are classified as emerging materials due to their optical properties for wastewater treatment. Among the aforementioned visible light catalysts, bismuth oxyhalides are considered as very promising due to their excellent photocatalytic activity owing to their good optical and electrical properties.[32] Among the bismuth ternary metal oxides, bismuth oxyiodide (BiOI) has the narrowest band gap and highest photocorrosion stability. It is also equipped with the strongest absorption under visible light and exhibits the best photoactivity.[33,34] Despite the possession of a narrow band gap and visible light absorption range properties, BiOI is plagued with the problem of increased recombination of photogenerated e^-/h^+, which affects its quantum efficiency. In view of this, adequate tailoring is mandatory to enhance the photoactivity of BiOI.

WO_3 is an n-type semiconductor that was chosen as the semiconductor to be etched into ZnO because of its promising physical and chemical properties. It possesses a narrow bandgap (2.4–2.8 eV) when compared to that of ZnO (3.2–3.37 eV), which enables it to absorb visible light. This property makes it an ideal candidate for photocatalysis. WO_3 is equipped with excellent photosensitivity, stability and resistance against photocorrosion in aqueous medium, remarkable electron mobility (6.5 $cm^2\ V^{-1}\ s^{-1}$) and good electron storage properties.[35,36] In addition, it is cost-effective, relatively harmless, exhibits fine interactions with metals, and has high mechanical strength. The ionic radius of WO_3 (0.062 nm) is very close to that of ZnO (0.074 nm), which makes it fit perfectly and inhibit the growth of the crystal sizes. Despite all of the interesting properties of WO_3, studies show that it is difficult to observe spontaneous H_2 formation with WO_3 without modification. This is attributed to the location of its lower CB edge [+0.5 V *vs.* NHE (normal hydrogen electrode) at pH = 0] with reference to the

standard H^+/H_2 redox level, in addition to the problem of the rapid recombination of photogenerated electrons and holes.[37]

Consequently, BiOI, being a p-type semiconductor with absorption in the visible range, is ideal for forming a p–n heterojunction with ZnO, which has absorption properties in the UV range. Coupling BiOI and ZnO will be an effective way to improve the photocatalytic activity. Furthermore, the relative energy of the WO_3 conduction band electrons limits its oxygen reduction capacity, and this leads to the build-up of these electrons, culminating in a reduced photocatalytic activity.[38] As a result of these limitations, the optimum utilization of WO_3 as a photocatalyst without any modification is inefficient. To enhance the photocatalytic performance of WO_3, incorporation of other dopants will be necessary.[36]

Polychlorinated biphenyls (PCBs) are synthetic compounds that have been detected in nearly every part of the global environment as pollutants, including water, sediments, air, fish and animals, and human adipose tissue, milk, and serum.[39] Among the class of pollutants listed as persistent organic pollutants (POPs), polychlorinated biphenyls are among the 12 persistent organic pollutants (POP) compounds, together with the 209 PCB congeners.[40] Originally, PCBs were abated by biodegradation, physical processes (such as incineration, solvent extraction, and adsorption), and chemical processes (such as the use of nanoscale zero-valent iron *via* dechlorination).[41–46] Incineration leads to the production of toxic by-products, such as polychlorinated dibenzo-p-dioxins and polychlorinated dibenzo-furan. Bioremediation is unsuitable because of the highly oxidized and recalcitrant nature of PCBs to biological processes. Adsorption requires large quantities of adsorbents, and may cause waste disposal problems and inefficient regeneration of the adsorbent. Some researchers have proposed sorption onto activated carbon, followed by thermal treatment of the solid residue, or super critical oxidation. However, these methods may not be cost-effective.[47–49] Photocatalysis has been proposed for the treatment of PCBs. However, there are not many literature reports in this regard. The pollutant of interest in this study is 2-chlorobiphenyl (2CBP), which was chosen because 2CBP is one of the PCB congeners with the highest solubility in aqueous media. This makes it one of the most probable PCBs to occur in aqueous environments. In light of the observed chemical and biological stabilities of 2CBP, photocatalytic degradation could be an important route for its environmental abatement.[50]

Some other studies have synthesized heterostructures *via* different procedures, such as plasma synthesis, ultra sound method, mechanochemical technique, and facile mechanical mixing method.[51–54] In this study, a series of bare photocatalysts and varying combinations of ZnO-[*X*]WO_3 and ZnO-[*X*]BiOI were synthesized *via* direct and facile methods to obtain a series of photocatalysts and heterostructures (ZnO, WO_3, BiOI, ZnO-[5%]WO_3, ZnO-[10%]WO_3, ZnO-[20%]WO_3, ZnO-[5%]BiOI, ZnO-[10%]BiOI, ZnO-[20%]BiOI). These prepared semiconductor photocatalysts and heterostructures were applied in the destruction of 2-chlorobiphenyl. The degradation reactions were fitted to the pseudo-first and second order kinetic models to exploit the kinetic process of the photodegradation reaction. A charge separation mechanism has been proposed. Previous studies have worked with very low concentrations due to the chemical stability, difficulty, and difficult degradation mechanism of 2-CBP.[55,56] For example, Hong *et al.* (1998) used 1 ppm in their study, Huang *et al.* (1996) worked with a concentration of 265 ppb, Carey *et al.* (1976) experimented at 25 ppb, while Zhang *et al.* (1993) conducted their study at 80 ppb.[50,56–58] In this study, a concentration of 10 ppm was chosen, which is both interesting and challenging.

2. Materials and methods

2.1. Materials

Potassium iodide (KI), bismuth nitrate pentahydrate ($Bi(NO_3)_3 \cdot 5H_2O$), ammonium metatungstate ($(NH_4)_6H_2W_{12}O_{40}$), oxalic acid, and 2-chlorobiphenyl (2CBP) were purchased from Sigma-Aldrich. ZAD [$(Zn(CH_3COO)_2 \cdot 2H_2O)$], ethanol and methanol were purchased from Associated Chemical Enterprises (ACE). Deionized water purified by a Millipore system was used for all sample preparations. All solvents and chemicals used in the experiments were of AR grade, and therefore not subjected to any additional purification before use. A stock solution of 1000 ppm 2CBP was prepared in a methanol–water ratio of 85 : 15 under vigorous and continuous stirring. Further dilutions of the stock solution were used to obtain the desired concentrations of 10 ppm for this study.

2.2. Preparation of ZnO, WO_3, BiOI, ZnO-(*X*)WO_3 and ZnO-(*X*)BiOI

ZnO nanoparticles were synthesized *via* a sol–gel process. ZAD [$Zn(CH_3COO)_2 \cdot 2H_2O$] was used as the precursor, ethanol as the solvent and oxalic acid as the surfactant. ZAD was dissolved in a beaker containing ethanol, which was subsequently poured into a 3-neck reactor set on a reflux apparatus and water bath. The solution was refluxed at 60 °C (±5) under vigorous stirring for 30 minutes. A clear solution was obtained. Oxalic acid (12.5 g) was dissolved in a beaker containing ethanol, and was subsequently added "dropwise" into the ZAD solution. On addition of oxalic acid, the formation of gels was observed as reflux was continued at 50 °C (±5) for 60 minutes. After refluxing, the xerogel was cooled to ambient temperature and oven dried overnight at 80 °C. After drying, the sample was collected and calcined at 500 °C in a furnace to obtain the ZnO nanoparticles.

Tungsten trioxide (WO_3) nanoparticles were synthesized *via* a simple hydrothermal process. Ammonium metatungstate hydrate powder (AMT) was dissolved in deionized water, and stirred for a few minutes. The solution was transferred to a hydrothermal autoclave reactor, and put into an oven at 120 °C for 18 hours. The sample was taken out of the autoclave after the reaction and filtered off, washed with water, and then washed with ethanol. The filtered product was dried in ambient air, and subsequently calcined in a furnace at 500 °C for 2 hours to obtain the WO_3 nanoparticles.

BiOI nanoplates were synthesized *via* a facile hydrothermal process. Bismuth nitrate pentahydrate ($Bi[NO_3]_3 \cdot 5H_2O$) and potassium iodide (KI) were utilized as precursors in this

synthesis. Bismuth nitrate pentahydrate was dissolved in 60 ml of ethanol and stirred for 30 minutes. Potassium iodide was dissolved in 60 ml of deionized water separately, and also stirred for 30 minutes. The KI solution was introduced dropwise into the bismuth nitrate pentahydrate solution as stirring was continued for 60 minutes. The reddish-brown solution was subsequently transferred to a hydrothermal autoclave reactor, and placed in an oven at 130 °C for 18 hours. The autoclave was taken out of the oven and allowed to cool to avoid the release of iodine gas. The suspension was poured onto a filter paper in a glass funnel, and washed with water and alcohol. Deionized water and alcohol were used to rinse the Teflon of the autoclave. Deionized water was lastly used to wash off traces of alcohol on the filter paper. The product on the filter paper was dried and subsequently ground in agate mortar to obtain the BiOI nanoplates.

To synthesize a ZnO–WO_3 heterojunction of different weight percentages (5, 10, 20%), ZnO was dispersed in deionized water and stirred for 30 minutes. Ammonium hydroxide was used to maintain the pH of the mixture at 6.5. A stoichiometric amount of ammonium metatungstate hydrate $[(NH_4)6H_2W_{12}O_{40}]$ was introduced to the mixture, and left to stir for 15 hours. The precipitate formed was filtered, washed several times with deionized water and ethanol, and subsequently air dried. The dried sample was collected, ground in an agate mortar, and subsequently calcined at 500 °C for 3 hours to obtain the ZnO-[*X*]WO_3 heterojunction.

To synthesize ZnO-[*X*]BiOI, ZnO was suspended in deionized water. A stoichiometric amount of bismuth nitrate pentahydrate $[Bi(NO_3)_3 \cdot 5H_2O]$ was added to ethanol under vigorous stirring. The latter was poured into the suspension and stirring was continued. A stoichiometric amount of potassium iodide (KI) was dissolved in deionized water, and added dropwise into the mixed liquor under vigorous and continuous stirring. The mixed liquor was allowed to stir for 3 hours. The suspension was subsequently centrifuged at 4000 rpm for 15 minutes, and dried in ambient air for 18 hours. The dried product was collected and ground in an agate mortar to obtain a series of ZnO–BiOI heterojunctions.

2.3. Characterization

The surface morphologies and elemental analysis of the as-synthesized composites were determined using a Carl Zeiss Sigma FE-SEM equipped with an Oxford X-act EDS. Optical studies were conducted using a UV 1800 Shimadzu UV-vis Spectrophotometer. X-ray diffraction measurements were made with a Bruker D2 XRD instrument, while BET surface area measurements and isotherms were obtained using a Micrometrics TriStar 3000 instrument. The average particle sizes of the as-synthesized composites were calculated from diffraction peaks using the Debye–Scherrer relation, while band gap was calculated *via* Tauc plots established from UV-vis spectra. A Hettich ROTOFIX Benchtop Centrifuge was used to separate some particles suspended in liquids during synthesis, while all pH values were determined using an OHAUS Starter 3100 pH meter. The light source for this study was an AM 1.5G 100 mW cm^{-2} lamp.

The model pollutant (2-CBP) was analyzed using a Shimadzu GC-MS QP 2010 equipped with a Rxi-5ms column of 30 m length, an internal diameter of 0.25 mm and a film thickness of 0.25 μm. Helium was used as the carrier gas, and the injector temperature was set at 220 °C. A volume of 1 μl of sample was auto-injected into the column. The temperature program was set at 140 °C, held for 4 minutes and then ramped up to 240 °C at a rate of 4 °C min^{-1}, and subsequently held for 10 minutes. The GC run was initiated after 3 minutes to isolate the solvent peak from the chromatogram because of the solvent cut-off point. The compound of interest was identified between 4 minutes to 10 minutes.

2.4. Photocatalytic evaluation

The degradation of 2-chlorobiphenyl under simulated solar radiation was used to assess the photo-activities of the composite photocatalysts and heterostructures. A stock solution of 1000 ppm 2CBP was prepared in a methanol–water ratio of 85 : 15 under vigorous and continuous stirring. Further dilutions of the stock solution were used to obtain the desired concentrations of 10 ppm for this study. A concentration of 10 ppm of 2CBP in 100 ml solvent solution was placed in a beaker, mounted on a stirrer plate, and placed directly under the light source. The initial concentration was taken into account. The desired amount of catalyst was introduced thereafter, and magnetically stirred in the dark for 30 minutes. This was to enable the establishment of equilibration of adsorption–desorption between the pollutant and the surface of the photocatalyst. During the experiments, the suspensions were magnetically stirred to properly disperse the photocatalysts. The pH values of the respective experiments were adjusted using HCl and NH_4OH. The photocatalytic activities of the individual photocatalysts were evaluated using an AM 1.5G 100 mW cm^{-2} solar radiation simulator. The surface of the beaker was covered in order to prevent the escape of radiation during the photocatalytic process. At designated time intervals, 3 ml aliquots of the mixture were taken out using a syringe and filtered using a 0.22 μm simplepure membrane filter attached to the syringe. This was done to separate the photocatalyst particles. After irradiation, the filtered samples were equilibrated in a dark box lined with aluminum foil and stored in the refrigerator prior to GC analysis.

3. Results and discussion

3.1. X-ray diffraction

The XRD pattern of the as-prepared ZnO nanoparticles shows sharp and intense peaks observed at 2θ values of 31.7°, 34.4°, 36.1°, 47.3°, 56.3°, 62.6°, 66.3°, 67.9° and 69.1°, which correspond to the 100, 002, 101, 102, 110, 103, 200, 112 and 201 crystal planes of hexagonal ZnO, respectively. As displayed in Fig. 1, the diffraction peaks of pure ZnO are intense and narrow, showing the high crystalline character. The orientation of the as-synthesized ZnO nanoparticles conformed to the hexagonal

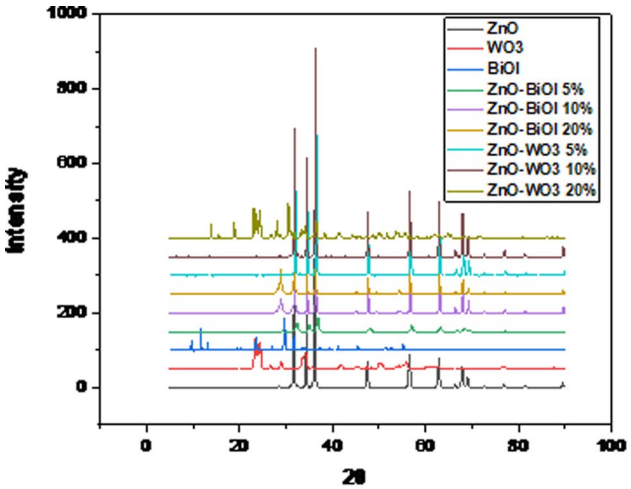

Fig. 1 XRD patterns of the as-prepared bare photocatalysts and heterostructures.

wurtzite phase of pure ZnO nanoparticles, as indexed on JCPDS 01-075-6445. The diffraction peaks of the BiOI composite sample are classified as the tetragonal phase of BiOI, and indexed on the JCPDS card number 00-010-0445. From the displayed pattern, it is observed that the sample contains the pure phase of BiOI coexisting with mixed phases, such as Bi_5O_7I and $Bi_7O_9I_3$. This is attributed to the synthesis method and the long hydrothermal reaction time in the autoclave lined with a Teflon. The peaks located at 10°, 30°, 34°, 46°, and 56° correspond to the identified (001), (102), (110), (200), and (212) diffraction planes, respectively. The intense and sharp diffraction peaks of the sample indicate the high crystallinity of the as-synthesized photocatalyst. The XRD pattern of the WO_3 sample (as shown in Fig. 1) corresponds to the triclinic phase of tungsten trioxide, as indexed on JCPDS card number 00-032-1395. There are no observed impurity peaks, which attest to the purity of the sample and excellent synthesis. Peaks were identified at 23.26°, 24.47°, 26.79°, 28.95°, 34.20°, 49.98°, and 55.89° and correspond to the 001, 110, 101, 200, 201, 220 and 202 crystal planes, respectively. The pattern for the sample with 5% BiOI loading does not show peaks of BiOI within the ZnO lattice. This could be due to the detection limit of the instrument, which is also related to the low loading of BiOI on the ZnO surface. This occurrence is also ascribed to the high dispersion of BiOI on the surface of ZnO. At 10% loading, a peak at 29° appeared, which corresponds to the 102 diffraction plane of BiOI nanoparticles. At an increased loading of 20%, the peak at 29° became more intense. This confirmed the increased loading of BiOI and its complete integration within the ZnO lattice. The intensity of the peaks increased with increased loading of BiOI. The XRD patterns of the as-prepared heterojunctions exhibited characteristic peaks of both pure BiOI and ZnO crystalline phases. There were no other impurity peaks observed in all three samples, which confirms the purity of the samples, excellent synthesis, and complete dispersal of BiOI on the surface of the ZnO nanoparticles. Fig. 1 also shows the XRD patterns of the as-prepared ZnO–WO_3 composites with different WO_3 loadings. All of the samples can be indexed to the triclinic phase of WO_3 and typical hexagonal wurtzite structure of pure ZnO samples. The intensity of the peaks increased with increased loading of WO_3 in the ZnO lattice. The samples with 5% and 10% loading of WO_3 do not show any peaks apart from the peaks of ZnO. This can be attributed to the detection limit of the instrument, as well as good dispersal of WO_3 on the surface of ZnO. At an increased loading of 20%, intense peaks were observed at 23°, 24.4°, 28° and 34°, corresponding to the 001, 110, 200 and 201 crystal planes of triclinic WO_3, respectively, in addition to the characteristic peaks of hexagonal ZnO. No impurity peaks were observed, which shows physical content homogenization in all of the composites. The average crystallite sizes of all of the synthesized photocatalysts were calculated from the FWHM obtained from the diffraction peaks using the Debye–Scherrer equation:

$$D = K[(\lambda/(\beta \cos \theta)] \quad (1)$$

where $\lambda = 1.54056$ nm is the wavelength of X-ray diffraction used, θ is the Bragg diffraction angle of the XRD peak, and β is the measured broadening diffraction line peak at an angle 2θ at half its maximum intensity (in radian).

The calculated crystallite sizes of the composites are presented in Table 1. The average crystallite sizes of ZnO, BiOI and WO_3 were calculated as: 37.6, 40 and 13 nm, respectively. The heterostructure with 5% BiOI had an average crystallite size of 16.4 nm, and the sample with 10% BiOI had an average crystallite size of 31 nm, while the sample with 20% BiOI loading had an average crystallite size of 45 nm. The average crystallite size increased with increased loading of BiOI in the ZnO composite. There may have been a penetration of the hexagonal wurtzite crystal structure of ZnO by tetragonal BiOI, which would influence the crystal growth-induced collapse. This occurrence explains the small crystallite size of the 5% ZnO–BiOI compared to the other samples. This also explains the increased crystallite size in the other samples. The sample with 5% loading of WO_3 had an average crystallite size of 35.4 nm, while the sample with 10% WO_3 content had an average crystallite size of 49 nm. The sample with 20% loading of WO_3 was estimated to have an average crystallite size of 31 nm.

Table 1 Average crystallite sizes of the bare photocatalysts and heterostructures

Sample	FWHM	Average crystallite size (nm)
ZnO	0.2295	37.6
WO_3	0.6533	12.9
BiOI	0.2068	40.0
ZnO-BiOI 5%	0.5276	16.4
ZnO-BiOI 10%	0.2797	31.0
ZnO-BiOI 20%	0.1887	45.0
ZnO-WO_3 5%	0.2441	35.4
ZnO-WO_3 10%	0.1759	49.0
ZnO-WO_3 20%	0.2687	31.0

3.2. SEM-EDS analysis

The morphologies of the ZnO, WO_3, BiOI, ZnO-(*X*)BiOI and ZnO-(*X*)WO_3 composites were investigated using FE-SEM. As shown in Fig. 2a, there is an observed high porosity with a sponge-like morphology and agglomeration due to the elevated temperature chemical reactions (500 °C) for the ZnO nanoparticles. This resulted in a dense morphology due to the total decomposition of the organometallic precursor. Scanning electron microscopy of the as-synthesized BiOI catalyst showed an irregular shaped plate-like morphology, as seen in Fig. 2b. The type of solvents used for the synthesis may have played a role in the observed morphology, in addition to the hydrothermal method used. The

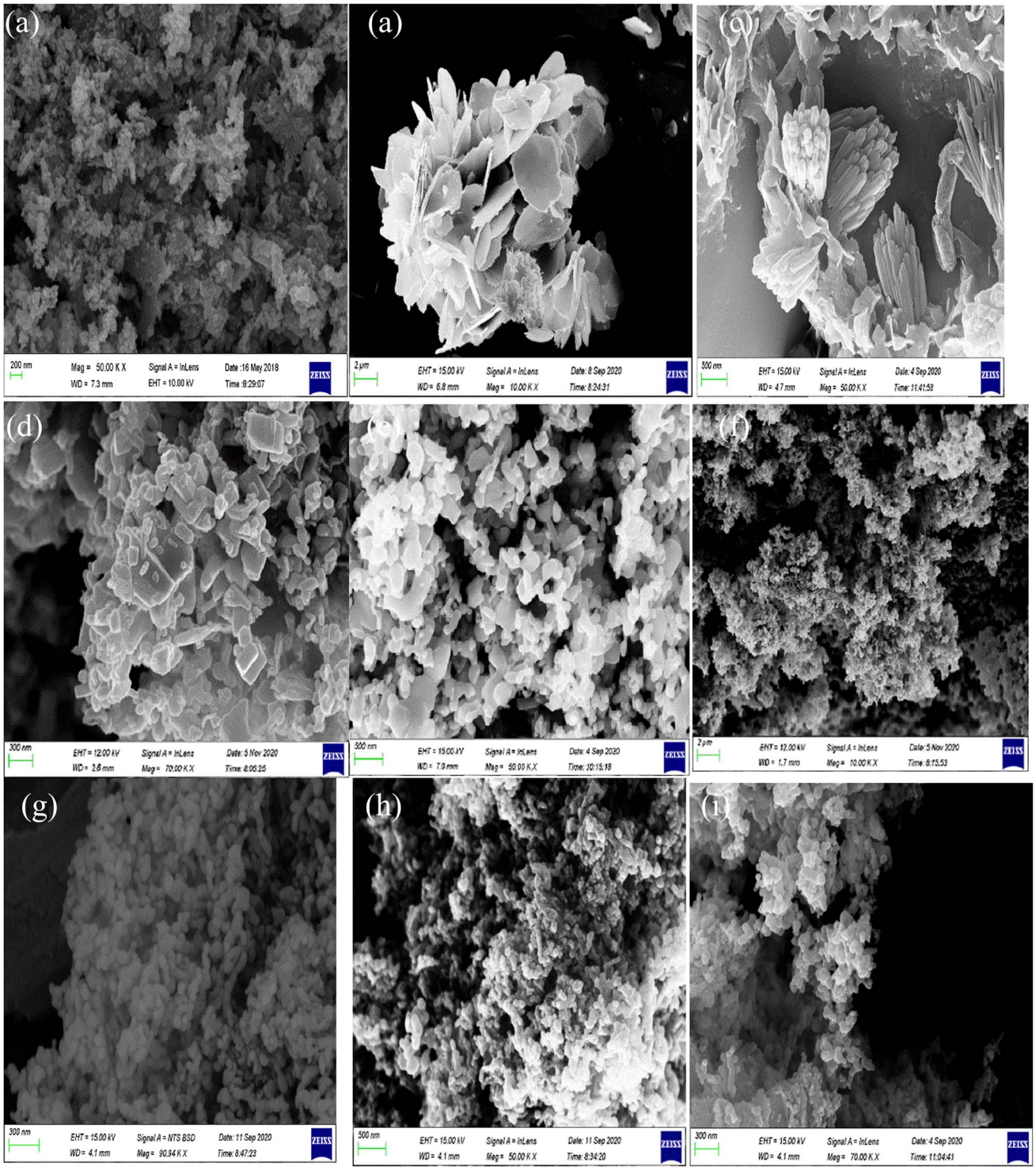

Fig. 2 SEM images of (a) ZnO, (b) BiOI, (c) WO_3, (d) ZnO-[5%]BiOI, (e) ZnO-[10%]BiOI, (f) ZnO-[20%]BiOI, (g) ZnO-[5%]WO_3, (h) ZnO-[10%]WO_3, and (i) ZnO-[20%]WO_3.

low viscosity solvents used in the synthesis process contributed to the plate-like morphology due to the high diffusion rate of the ions. The Yusoff group in 2019 also observed a plate-like morphology after the direct crushing of $Bi(NO_3)_3 \cdot 5H_2O$ and KI, subsequent addition of distilled water to form a paste.[59] Fig. 2c shows the SEM image of the WO_3 nanoparticles. There is a combination of highly agglomerated non-homogeneous nanorod assays and pointed end morphology. This can be attributed to the long reaction time in the autoclave and subsequent calcination at elevated temperature. Tehrani and colleagues (2020) also observed the same effect in their study, which used $Na_2WO_4 \cdot 2H_2O$, sodium sulphate and citric acid as starting materials.[60] The reaction time of 18 hours in the Teflon-lined autoclave and a calcination temperature of 500 °C hours may have caused the agglomeration. The SEM images of the ZnO–BiOI heterojunctions (5%, 10%, 20%) show changes in the morphology of ZnO. The images show non-uniform surfaces. With increased loading of BiOI on ZnO, one can observe penetration of the rods and rectangular plates with reference to 5% (Fig. 2d) loading of BiOI. At 10% (Fig. 2e) loading, there seemed to be more penetration and onset of agglomeration with irregularly shaped aggregates and some plates. The sample with 20% (Fig. 2f) loading showed more agglomeration, resulting in a sponge-like morphology with pores, which could be as a result of further wrapping between ZnO and BiOI aggregates. From these observations, it can be deduced that the morphology very much depends on the loading of BiOI in the heterostructures. Scanning electron microscopy of the various loadings of WO_3 on the ZnO nanoparticles shows agglomeration with no particular uniform morphology, as seen in Fig. 2g–i. From close observation, mostly nodular morphology can be identified for all three samples. As loading of the WO_3 increased in ZnO, more agglomeration was observed. This can be attributed to the preparation method and starting materials, which may have caused highly dense clusters of small grains that are interconnected. The sample containing 20% wt. WO_3 exhibited the highest level of agglomeration. Generally, the morphologies of all three samples do not show remarkable changes with increased loading when it is compared to the SEM images of pure ZnO and WO_3. Lei and colleagues (2019) also observed the same outcome in their synthesis, which combined hydrothermal and impregnation processes, followed by subsequent calcination.[61]

The energy dispersive X-ray spectra of the composites are shown in ESI 1a–i.† The EDS analysis confirm the presence of only the reference elements, in addition to the appropriate stoichiometry.

3.3. Optical properties

A UV-vis spectrophotometer was used to determine the absorption properties of the composites. All spectra were recorded at room temperature in the range of 200–900 nm. The bandgaps of all the composites were calculated from Tauc's plots *via* the Kubelka–Munk equation (Eqn (2)) by extrapolating the linear portion of the plot of $(\alpha h\nu)^2$ *vs.* the photon energy, as shown in the equation below:

$$\alpha h\nu = A(h\nu - E_g)^n \quad (2)$$

where α is the absorption coefficient, A is a constant, h is Plank's constant, ν is the photon frequency, E_g is the band gap, and n is equal to 1/2 or 2 for the transition being direct or indirect, respectively. Extrapolating the linear region in a plot of $(\alpha h\nu)^2$ against $h\nu$ gives the band gap values.

The absorption spectra and Tauc plots of the composites are shown in ESI 2a–h.† From the absorption spectra, the absorbance of ZnO, BiOI, WO_3, ZnO-[5%]BiOI, ZnO-[10%]BiOI, ZnO-[20%]BiOI, ZnO-[5%]WO_3, ZnO-[10%]WO_3 and ZnO-[20%]WO_3 were observed at 373, 371, 465, 376, 378, 380, 376, 377 and 380 nm, respectively. The absorption tail of BiOI was observed beyond 600 nm, similar to the same observation made by Qu and colleagues (2020).[62] WO_3 also had an absorption tail in the visible region. This property has been attributed to of the presence of pentavalent tungsten (W^{5+}) on the surface of the nanoparticles, which has broad absorption in the visible region as a result of the capture of photo-excited electrons at WO_3 trapping sites.[63] Slight red shifts were observed in all of the heterostructures.

The bare photocatalysts (ZnO, BiOI, WO_3) had calculated band gap values of 3.24, 1.23 and 2.4 eV, respectively. A narrowing of the band gaps was observed for the ZnO-(*X*)BiOI heterostructures as the BiOI loading increased. With reference to the pure ZnO, the band gap was observed at 3.24 eV. However, with the introduction of BiOI at 5% loading, the band gap narrowed down to 3.08 eV. As the BiOI loading was increased to 10%, the band gap further narrowed to 3.0 eV. The composite with the highest BiOI loading at 20% showed the highest band gap narrowing, as the band gap was estimated at 2.20 eV. This observation corresponds to the associated red shift for the absorbance of each of the composites. The ZnO-[5%]WO_3 composite had an estimated band gap of 2.56 eV, showing band gap narrowing from the already established band gap of ZnO (3.24 eV). As the WO_3 loading was increased to 10%, there may have been a formation of energy level defects in the forbidden band, as the band gap was estimated to be 3.16 eV. This is greater than the band gap of the ZnO-[5%]WO_3 composite, but still lower than the band gap of the undoped ZnO. This also explains the further band gap narrowing of the ZnO-20% WO_3 composite, which was observed to have the narrowest band gap of 2.17 eV. The same observation was made in the study by Adhikari and colleagues.[18]

3.4. Textural properties

The surface area of the as-synthesized photocatalysts were measured using the standard nitrogen adsorption–desorption isotherm and the Barret-Joyner-Halender (BJH) pore distribution curves. From the nitrogen adsorption–desorption isotherm analysis, the results were compared with the IUPAC classification.

The specific surface area of ZnO, BiOI, WO_3, ZnO-[5%]BiOI, ZnO-[10%]BiOI, ZnO-[20%]BiOI, ZnO-[5%]WO_3, ZnO-[10%]WO_3 and ZnO-[20%]WO_3 were measured as 1.93, 2.61, 1.08, 7.31,

Table 2 Textural properties, band gaps and degradation efficiency

Catalyst	S_{BET} (m^2 g^{-1})	Pore volume (cm^3 g^{-1})	Pore-size (nm)	Bandgap (eV)	Degradation (%)
BiOI	2.61	0.019	26.0	1.23	49
WO_3	1.08	0.014	43.2	2.4	28
ZnO	1.93	0.012	25.7	3.24	20
ZnO-WO_3 5%	7.84	0.042	20.3	2.56	45
ZnO-WO_3 10%	5.69	0.021	24.5	3.16	53
ZnO-WO_3 20%	5.57	0.042	32.0	2.17	33
ZnO-BiOI 5%	7.31	0.064	31.0	3.08	7
ZnO-BiOI 10%	19.79	0.180	35.0	3.0	56
ZnO-BiOI 20%	7.30	0.534	31.5	2.20	28

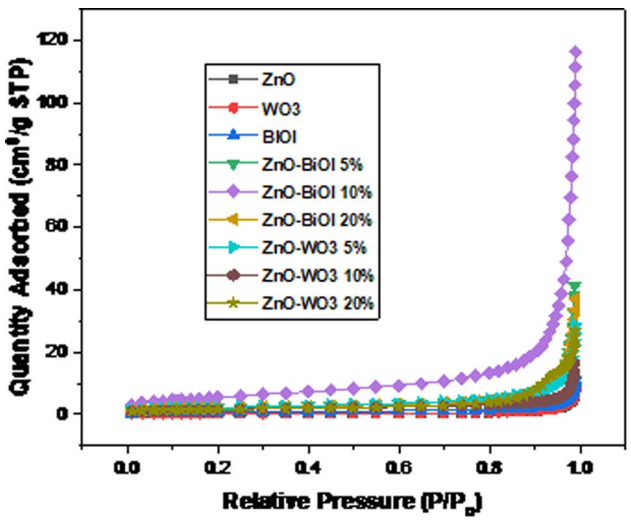

Fig. 3 N_2 adsorption–desorption isotherms of the as-prepared bare catalysts and heterostructures.

19.79, 7.30, 7.84, 5.69, 5.57 m^2 g^{-1}, respectively, as presented in Table 2.

The N_2 adsorption–desorption isotherms (Fig. 3) showed that nearly all of the as-synthesized composites were mesoporous and displayed Type IV isotherms. The one exception was ZnO, which exhibited a Type V isotherm. In addition, most of the isotherms did not exhibit any hysteresis, except for ZnO, ZnO-[20%]BiOI, ZnO-[20%]WO_3 and WO_3, which exhibited type H_{III} hysteresis. The Barret-Joyner-Halender (BJH) pore size distribution curves of the isotherms indicated a mixture of mesopores and macropores, with ZnO-[5%]BiOI and ZnO-[10%]BiOI showing more macropores than mesopores in the tested materials, as shown in Fig. 4. The surface area measurements increased with the construction of heterojunctions. However, these increments did not follow any particular trend.

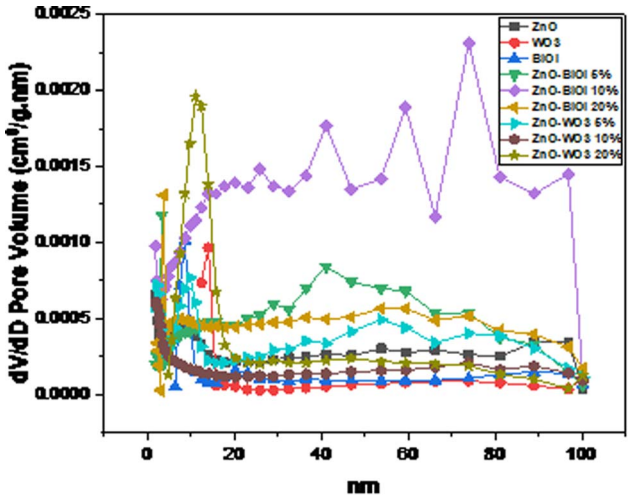

Fig. 4 Barret-Joyner-Halender (BJH) pore size distribution of the as-prepared bare catalysts and heterostructures.

3.5. Photocatalytic protocol

The photocatalytic performance of the as-synthesized bare photocatalysts and heterostructures were evaluated by the photodestruction of 2-chlorobiphenyl (2CBP). Fig. 5a and b show the degradation efficiencies and photodegradation plots of 2CBP by the as-prepared composites. All of the photocatalysts showed varying degrees of photocatalytic efficiencies. Bare ZnO achieved an efficiency of 20% at 150 minutes, while bare WO_3 achieved 28% destruction at the same time. BiOI was observed to be the most efficient catalyst (49%) among all of the bare catalysts. The heterostructures comprising ZnO-[5%]BiOI, ZnO-[10%]BiOI, ZnO-[20%]BiOI, ZnO-[5%]WO_3, ZnO-[10%]WO_3 and ZnO-[20%]WO_3 exhibited varying photocatalytic activities as the observed efficiencies were 7%, 56%, 28%, 45%, 53% and 33%, respectively, as shown in Fig. 5a. The photocatalytic activities of the bare/undoped photocatalysts follow the trend BiOI > WO_3 > ZnO. This is attributed to the quick separation of the electron–hole pairs, before recombination takes place. In addition, BiOI was observed to possess the narrowest band gap among the bare photocatalysts. This may have contributed to its photocatalytic performance.

The fabricated heterojunctions containing 5% loading of BiOI and WO_3 showed diverse results. The composite containing 5% WO_3 (45%) showed significant activity when compared to its 5% BiOI (7%) counterpart, coupled with its slightly larger surface area. The samples loaded with 20% BiOI/WO_3 also showed varying photocatalytic activities, although the difference in efficiencies is not as significant as the composites with 5% loading. At similar reaction conditions, ZnO-[20%]WO_3 and ZnO-[20%]BiOI achieved degradation efficiencies of 33% and

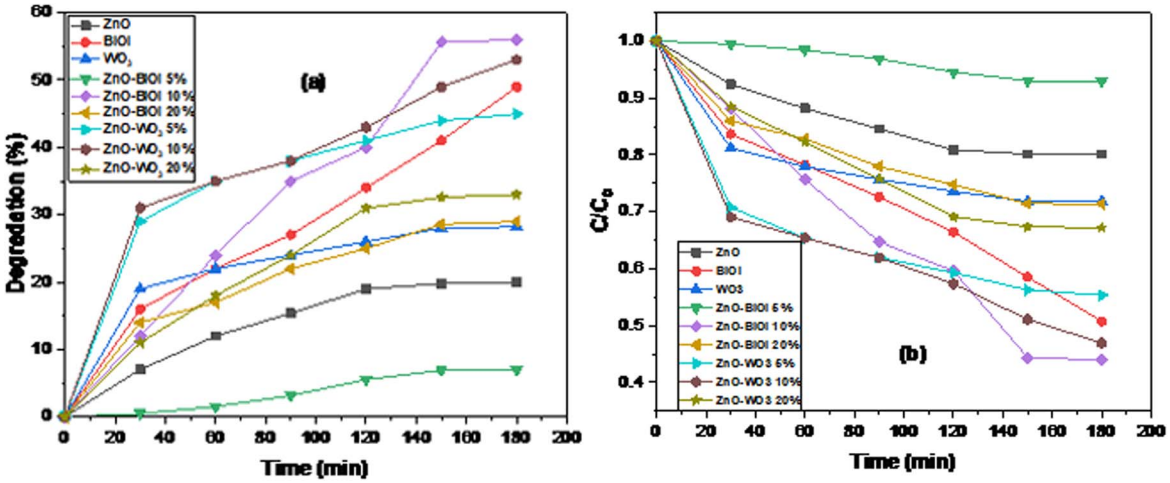

Fig. 5 Photodegradation plots of (a) degradation efficiency, and (b) time-dependent photocatalytic degradation.

28%, respectively. The composites of ZnO-[10%]BiOI and ZnO-[10%]WO_3 were observed to be the photocatalysts with the most significant activities in this study. ZnO-[10%]BiOI (56%) achieved approximately two-fold the efficiency of ZnO-[20%]BiOI (28%), while ZnO-[10%]WO_3 (53%) showed much more significant activity than ZnO-[20%]WO_3 (33%). Loading at 20% (BiOI, WO_3) onto the bare ZnO showed a significant reduction in photocatalytic activity. This may have been caused by the excessive loading, which leads to the formation of recombination centers and light penetration depth that exceeded the space charge layer, leading to quick recombination of the photogenerated electron–hole pairs.[64]

The composite (ZnO-[10%]BiOI) with the largest surface area (19.79 m^2 g^{-1}) and a significant pore volume was observed to exhibit the best photocatalytic activity. Heterogeneous photocatalysis is mostly efficient when a photocatalyst is equipped with a large surface area. As already established, photocatalysis mainly occurs on the photocatalyst's surface.[65] Typically, a photocatalyst with a high number of atoms on its surface will have enhanced adsorption properties. Nanosized diameters of nano-structures will make charge separation of the photogenerated electrons and holes easier due to transfer of the charge carriers from the bulk to the surface of the photocatalyst. Thus, a larger surface area leads to the subsequent formation of more hydroxyl radicals for more photocatalytic reaction centers, even though our study did not follow that particular order. Several researchers made similar observations in their respective studies.[66–69] The as-synthesized composite in our study, which had the most significant and largest surface area, in addition to its significantly enhanced pore volume, exhibited the best photocatalytic activity in the destruction of 2CBP.

The construction of the ZnO-[10%]BiOI heterostructure enabled the spatial segregation of electrons and holes into different compartments, which in turn, encountered recombination and also isolated the redox sites on the surface of the photocatalyst. Incorporating semiconductors with different crystal structures and band positions results in more efficient utilization of incident photons, and leads to efficient charge separation by the electric field interface. This enhanced photoactivity of ZnO-[10%]BiOI is also attributed to increased light absorption and efficient charge separation, in addition to the narrow bandgap and exposed reactive facets. Thus, the BiOI in the heterostructure acted as a photosensitizer. Furthermore, coupling ZnO and BiOI into a heterojunction enhanced the photocatalytic activity of ZnO because of the high-contact areas enabled by the fast charge transfer channel of BiOI and ZnO, in addition to the presence of more active sites.[70] A decline in the photocatalytic activity was observed beyond the 20% loading of ZnO-WO_3 and ZnO-BiOI heterostructures because of a reduction in the separation efficiency of the photoinduced electrons and holes. Furthermore, loading BiOI beyond 20% is detrimental to the heterojunction because of the tendency of BiOI to aggregate and agglomerate.[71–73] Thus, ZnO-[10%]BiOI was identified as the optimal photocatalyst for this study.

3.6. Proposed degradation mechanism

The results obtained from the experiment give a strong indication that the superior photodegradation activity of the ZnO-[10%]BiOI nanocomposite is due to the p–n heterojunction structure between ZnO and BiOI.[71,73,74] From the UV-vis spectra of both ZnO and BiOI, the calculated band gaps were established as 3.24 eV and 1.23 eV, respectively. A simplified band energy structure of ZnO and BiOI is shown in Fig. 6. ZnO, being a typical n-type photocatalyst, has its Fermi level close to its conduction band. Meanwhile, being a p-type photocatalyst, BiOI has its Fermi level located close to its valence band.[8,33,74] The introduction of BiOI into the ZnO lattice and subsequent p–n heterojunction construction leads to the realignment of the Fermi levels of the two materials. This causes band bending and creation of electric fields.[75] Photoexcited electrons transfer to the conduction band of ZnO, leaving the holes in the BiOI valence band (Fig. 6b). This takes place because the conduction band of BiOI is more negative than the conduction band of ZnO. In the same way, the valence band of ZnO is more positive than

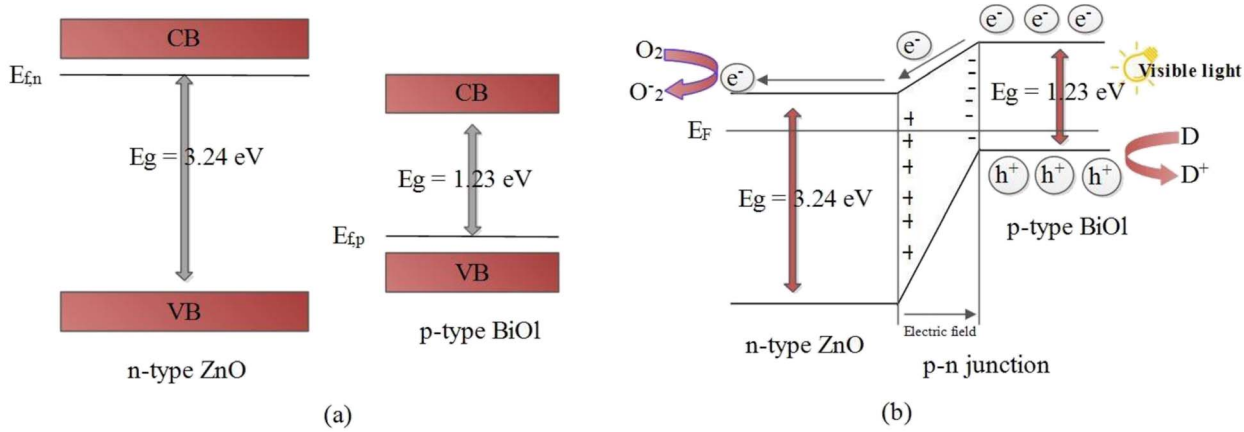

Fig. 6 Proposed band energy diagram of ZnO and BiOI before contact (a), and after (b) interfacial contact, formation of p–n junction and charge separation process of the ZnO–BiOI heterostructure under solar irradiation.

that of BiOI. This shows that separation efficiency of the ZnO-[10%]BiOI composite is improved. In turn, the photocatalytic activity is also improved.

The reduction of photocatalytic activity beyond the optimum doping of 10% is attributed to the excessive loading of BiOI onto ZnO and the reduction in number of active sites.[76] This may have caused BiOI to act as recombination centers, leading to reduced photocatalytic performance. Khatamian and colleagues attribute this to the light penetration depth, which exceeded the space charge layer.[77] This makes it easy for the photogenerated electron–hole pairs to recombine, leading to a lower photocatalytic performance. Thus, an optimum concentration of BiOI is mandatory to match the thickness of the charge layer and light penetration depth to effectively separate the photogenerated electron–hole pairs. Several studies have observed a similar trend.[18,78–80]

From the experimental results, the following photocatalytic mechanism is proposed:

$$\mathrm{BiOI} \xrightarrow{h\nu(\lambda \geq 400\ \mathrm{nm})} \mathrm{BiOI}\left(h^{+}_{\mathrm{VB}} + \mathrm{e}^{-}_{\mathrm{CB}}\right) \quad (3)$$

$$\mathrm{BioI}\left(\mathrm{e}^{-}_{\mathrm{CB}}\right) \xrightarrow{\text{transfer}} \mathrm{ZnO}\left(\mathrm{e}^{-}_{\mathrm{CB}}\right) \quad (4)$$

$$\mathrm{ZnO}(\mathrm{e}^{-}_{\mathrm{CB}}) + \mathrm{O_2} \rightarrow \mathrm{ZnO} + \mathrm{O_2}^{\bullet}- \quad (5)$$

$$\mathrm{O_2}^{\bullet -} + \mathrm{H}^{+} \rightarrow \mathrm{OH}^{\bullet} \quad (6)$$

$$\mathrm{O_2}^{\bullet -} \text{ and } \mathrm{OH}^{\bullet} + 2\mathrm{CBP} \rightarrow \text{degradation (products)} \quad (7)$$

3.7. Kinetics study

The 2CBP degradation data were fitted to the pseudo-first and second order kinetic models in order to exploit the kinetic process of the photodegradation reaction, as shown in Fig. 7a and b. It is observed that the experimental data could be fitted into both pseudo-first and second-order reaction kinetics models. The ZnO-[10%]BiOI heterophotocatalyst, which was the most efficient catalyst in this study, was observed to show the highest rate constants of 0.0054 min^{-1} and 0.0086 min^{-1} in

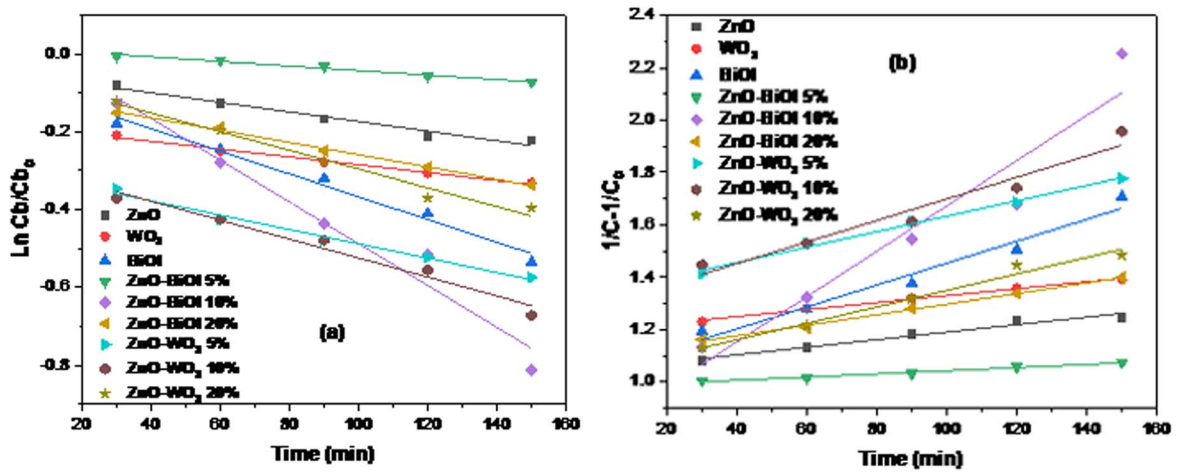

Fig. 7 (a) Pseudo-first-order kinetic model fit for 2-CBP degradation. (b) Pseudo-second-order kinetic model fit for 2-CBP degradation.

Table 3 Pseudo first and second order kinetics data for 2-CBP degradation by as-prepared photocatalysts and heterojunction composites

S/N	Photocatalyst	K (min^{-1})	R^2 ($\ln C_b/C_{bo}$)	$t_{1/2}$ (min)	R^2 ($1/C - 1/C_o$)	K_2 (L mg^{-1} min^{-1})
1	ZnO	0.0012	0.966	577.6	0.969	0.0014
2	WO_3	0.0010	0.990	693.1	0.993	0.0013
3	BiOI	0.0046	0.983	150.7	0.966	0.0041
4	ZnO-BiOI 5%	0.0005	0.983	1386.3	0.982	0.0006
5	ZnO-BiOI 10%	0.0054	0.964	128.4	0.922	0.0086
6	ZnO-BiOI 20%	0.0016	0.996	433.2	0.996	0.0020
7	ZnO-WO_3 5%	0.0036	0.987	192.5	0.993	0.0029
8	ZnO-WO_3 20%	0.0029	0.978	239.0	0.952	0.0031
9	ZnO-WO_3 10%	0.0049	0.969	141.5	0.981	0.0077

both first and second order kinetics models, respectively. When compared to undoped ZnO, the rate constant of the ZnO-[10%]BiOI heterostructure was observed to be nearly 5-fold higher. This further demonstrates the superior catalytic performance of the as-prepared ZnO-[10%]BiOI heterostructured photocatalyst. All of the photocatalysts and heterostructures showed increased rate constants in the second-order reaction kinetics model. In contrast, the rate constants of BiOI and ZnO-5% WO_3 decreased from 0.0046 to 0.0041 min^{-1} and 0.0036 to 0.0029 min^{-1}, respectively. The kinetic data show that it requires 128.4 minutes for the measured 2CBP concentration to be halved to the initial concentration when ZnO-[10%]BiOI is applied. The *R*-squared values affirm that the photocatalytic experiments in this study could follow both the pseudo-first and second order kinetic models. The rate constants and relative coefficients obtained by fitting the experimental data are listed in Table 3.

4. Conclusions

In this study, a series of bare photocatalysts and heterostructures were prepared for the photodestruction of 2-chlorobiphenyl. The ZnO-[10%]BiOI heterostructured photocatalyst exhibited superior photocatalytic activity in the destruction of 2CBP. The ZnO-[10%]BiOI heterophotocatalyst, which was the most efficient catalyst in this study, was observed to show the highest rate constants of 0.0054 min^{-1} and 0.0086 min^{-1} in both the first and second order kinetics models, respectively. When compared to undoped ZnO, the rate constant of the ZnO-[10%]BiOI heterostructure was observed to be nearly 5-fold higher. The kinetic data show that it requires 128.4 minutes for the measured 2CBP concentration to be halved to the initial concentration when ZnO-[10%]BiOI is applied. The findings from this study indicate that optimal creation of a heterojunction between ZnO and BiOI increases the photocatalytic activity and efficiency. The findings from this study suggest that ZnO-[10%]BiOI can potentially be used as an efficient and effective catalyst for the degradation of recalcitrant organic pollutants in water.

Conflicts of interest

No potential competing interest is reported by the authors.

References

1 H. Chen and L. Wang, Nanostructure sensitization of transition metal oxides for visible-light photocatalysis, *Beilstein J. Nanotechnol.*, 2014, **5**, 696–710.
2 L. V. Bora and R. K. Mewada, Visible/solar light active photocatalysts for organic effluent treatment: Fundamentals, mechanisms and parametric review, *Renewable Sustainable Energy Rev.*, 2017, **76**, 1393–1421.
3 J. García-Montaño, X. Domènech, J. A. García-Hortal, F. Torrades and J. Peral, The testing of several biological and chemical coupled treatments for Cibacron Red FN-R azo dye removal, *J. Hazard. Mater.*, 2008, **154**, 484–490.
4 M. Vinita, R. Praveena Juliya Dorathi and K. Palanivelu, Degradation of 2,4,6-trichlorophenol by photo Fenton's like method using nano heterogeneous catalytic ferric ion, *Sol. Energy*, 2010, **84**, 1613–1618.
5 G. Zelmanov and R. Semiat, Phenol oxidation kinetics in water solution using iron(3)-oxide-based nano-catalysts, *Water Res.*, 2009, **42**, 3848–3856.
6 M. Pirhashemi, A. Habibi-Yangjeh and S. Rahim Pouran, Review on the criteria anticipated for the fabrication of highly efficient ZnO-based visible-light-driven photocatalysts, *J. Ind. Eng. Chem.*, 2018, **62**, 1–25.
7 S. Meenakshisundaram, M. Muruganandham and S. Mika, Advanced Oxidation Processes for Wastewater Treatment, *Int. J. Photoenergy*, 2015, **2015**, 1–3.
8 M. Zhang, J. Qin, P. Yu, B. Zhang and M. Ma, Facile synthesis of a ZnO–BiOI p–n nano-heterojunction with excellent visible-light photocatalytic activity, *Beilstein J. Nanotechnol.*, 2018, **9**, 789–800.
9 D. Štrbac, C. A. Aggelopoulos, G. Štrbac, M. Dimitropoulos, M. Novaković, T. Ivetić and S. N. Yannopoulos, Photocatalytic degradation of Naproxen and methylene blue: Comparison between ZnO, TiO2 and their mixture, *Process Saf. Environ. Prot.*, 2018, **113**, 174–183.
10 T. V. A. Kusumam, T. Panakkal, T. Divya and M. P. Nikhila, Morphology controlled synthesis and photocatalytic activity of zinc oxide nanostructures, *Ceram. Int.*, 2016, **42**, 3769–3775.
11 S. Kaneco, N. Li, K. Itoh, H. Katsumata, T. Suzuki and K. Ohta, Titanium dioxide mediated solar photocatalytic

degradation of thiram in aqueous solution: Kinetics and mineralization, *Chem. Eng. J.*, 2009, **148**, 50–56.
12 D. Rajamanickam and M. Shanthi, Photocatalytic degradation of an organic pollutant by zinc oxide – solar process, *Arabian J. Chem.*, 2016, **9**, S1858–S1868.
13 M. I. Litter and J. A. Navio, Comparison of the photocatalytic efficiency of TiO2, iron oxides and mixed Ti(IV)Fe(III) oxides: photodegradation of oligocarboxylic acids, *J. Photochem. Photobiol., A*, 1994, **84**, 183–193.
14 T. Senasu and S. Nanan, Photocatalytic performance of CdS nanomaterials for photodegradation of organic azo dyes under artificial visible light and natural solar light irradiation, *J. Mater. Sci.: Mater. Electron.*, 2017, **28**, 17421–17441.
15 Z. Ye, L. Kong, F. Chen, Z. Chen, Y. Lin and C. Liu, A comparative study of photocatalytic activity of ZnS photocatalyst for degradation of various dyes, *Optik*, 2018, **164**, 345–354.
16 A. L. Linsebigler, G. Lu and J. T. Yates, Photocatalysis on TiO2 Surfaces: Principles, Mechanisms, and Selected Results, *Chem. Rev.*, 1995, **95**, 735–758.
17 T. T. Vu, L. del Río, T. Valdés-Solís and G. Marbán, Fabrication of wire mesh-supported ZnO photocatalysts protected against photocorrosion, *Appl. Catal., B*, 2013, **140–141**, 189–198.
18 S. Adhikari, D. Sarkar and G. Madras, Highly efficient WO3-ZnO mixed oxides for photocatalysis, *RSC Adv.*, 2015, **5**, 11895–11904.
19 E. Pelizzetti and C. Minero, Metal Oxides as Photocatalysts for Environmental Detoxification, *Comments Inorg. Chem.*, 1994, **15**, 297–337.
20 A. D. Mauro, M. E. Fragalà, V. Privitera and G. Impellizzeri, ZnO for application in photocatalysis: From thin films to nanostructures, *Mater. Sci. Semicond. Process.*, 2017, **69**, 44–51.
21 R. Ahmad, Z. Ahmad, A. U. Khan, N. R. Mastoi, M. Aslam and J. Kim, Photocatalytic systems as an advanced environmental remediation: Recent developments, limitations and new avenues for applications, *J. Environ. Chem. Eng.*, 2016, **4**, 4143–4164.
22 V. Scuderi, G. Impellizzeri, L. Romano, M. Scuderi, G. Nicotra, K. Bergum, A. Irrera, B. G. Svensson and V. Privitera, TiO2-coated nanostructures for dye photodegradation in water, *Nanoscale Res. Lett.*, 2014, **9**, 1–7.
23 W. S. Chiu, P. S. Khiew, M. Cloke, D. Isa, T. K. Tan, S. Radiman, R. Abd-Shukor, M. A. A. Hamid, N. M. Huang, H. N. Lim and C. H. Chia, Photocatalytic study of two-dimensional ZnO nanopellets in the decomposition of methylene blue, *Chem. Eng. J.*, 2010, **158**, 345–352.
24 M. Samadi, M. Zirak, A. Naseri, E. Khorashadizade and A. Z. Moshfegh, Recent progress on doped ZnO nanostructures for visible-light photocatalysis, *Thin Solid Films*, 2015, **605**, 2–19.
25 C. Tian, Q. Zhang, A. Wu, M. Jiang, Z. Liang, B. Jiang and H. Fu, Cost-effective large-scale synthesis of ZnO photocatalyst with excellent performance for dye photodegradation, *Chem. Commun.*, 2012, **48**, 2858–2860.
26 J. A. Anta, E. Guillén and R. Tena-Zaera, ZnO-Based Dye-Sensitized Solar Cells, *J. Phys. Chem. C*, 2012, **116**, 11413–11425.
27 S. Kuriakose, V. Choudhary, B. Satpati and S. Mohapatra, Enhanced photocatalytic activity of Ag–ZnO hybrid plasmonic nanostructures prepared by a facile wet chemical method, *Beilstein J. Nanotechnol.*, 2014, **5**, 639–650.
28 J. Kegel, I. M. Povey and M. E. Pemble, Zinc oxide for solar water splitting: A brief review of the material's challenges and associated opportunities, *Nano Energy*, 2018, **54**, 409–428.
29 S. G. Kumar and K. S. R. K. Rao, Comparison of modification strategies towards enhanced charge carrier separation and photocatalytic degradation activity of metal oxide semiconductors (TiO_2, WO_3 and ZnO), *Appl. Surf. Sci.*, 2017, **391**, 124–148.
30 S. G. Kumar and K. S. R. K. Rao, Zinc oxide based photocatalysis: Tailoring surface-bulk structure and related interfacial charge carrier dynamics for better environmental applications, *RSC Adv.*, 2015, **5**, 3306–3351.
31 A. O. Ibhadon and P. Fitzpatrick, Heterogeneous Photocatalysis: Recent Advances and Applications, *Catalysts*, 2013, **3**, 189–218.
32 M. Arumugam and M. Y. Choi, Recent progress on bismuth oxyiodide (BiOI) photocatalyst for environmental remediation, *J. Ind. Eng. Chem.*, 2020, **81**, 237–268.
33 J. Jiang, X. Zhang, P. Sun and L. Zhang, ZnO/BiOI Heterostructures: Photoinduced Charge-Transfer Property and Enhanced Visible-Light Photocatalytic Activity, *J. Phys. Chem. C*, 2011, **115**, 20555–20564.
34 H. Liu, J. Cai, M. Luo, C. Chen and P. Hu, Novel mesoporous bismuth oxyiodide single-crystal nanosheets with enhanced catalytic activity, *RSC Adv.*, 2020, **10**, 5913–5918.
35 X. Zhang, X. Lu, Y. Shen, J. Han, L. Yuan, L. Gong, Z. Xu, X. Bai, M. Wei, Y. Tong, Y. Gao, J. Chen, J. Zhou and Z. L. Wang, Three-dimensional WO_3 nanostructures on carbon paper: Photoelectrochemical property and visible light driven photocatalysis, *Chem. Commun.*, 2011, **47**, 5804–5806.
36 S. Singh, V. C. Srivastava and S. L. Lo, Surface Modification or Doping of WO_3 for Enhancing the Photocatalytic Degradation of Organic Pollutant Containing Wastewaters: A Review, *Mater. Sci. Forum*, 2016, **855**, 105–126.
37 P. Dong, G. Hou, X. Xi, R. Shao and F. Dong, WO3-based photocatalysts: morphology control, activity enhancement and multifunctional applications, *Environ. Sci.: Nano*, 2017, **4**, 539–557.
38 Y. Wicaksana, S. Liu, J. Scott and R. Amal, Tungsten trioxide as a visible light photocatalyst for volatile organic carbon, *Molecules*, 2014, **19**, 17747–17762.
39 S. Safe, Toxicology, Structure-Function Relationship, Human and Environmental Health Impacts of Polychlorinated Biphenyls: Progress and Problems, *Environ. Health Perspect.*, 1992, **100**, 259–268.
40 G. Li, L. Zhang and Z. Zhang, Determination of polychlorinated biphenyls in water using dynamic hollow fiber liquid-phase microextraction and gas

chromatography-mass spectrometry, *J. Chromatogr. A*, 2008, **1204**, 119–122.
41 W. Chu and C. Y. Kwan, Remediation of contaminated soil by a solvent/surfactant system, *Chemosphere*, 2003, **53**, 9–15.
42 A. P. K. Jantunen, A. A. Koelmans and M. T. O. Jonker, Modeling polychlorinated biphenyl sorption isotherms for soot and coal, *Environ. Pollut.*, 2010, **158**, 2672–2678.
43 P. E. Kubátová, I. Eichlerová, L. Homolka, F. Nerud and V. Šašek, PCB congener selective biodegradation by the white rot fungus Pleurotus ostreatus in contaminated soil, *Chemosphere*, 2001, **43**, 207–215.
44 Y. Wang, D. Zhou, Y. Wang, X. Zhu and S. Jin, Humic acid and metal ions accelerating the dechlorination of 4-chlorobiphenyl by nanoscale zero-valent iron, *J. Environ. Sci.*, 2011, **23**, 1286–1292.
45 R. Weber, T. Takasuga, K. Nagai, H. Shiraishi, T. Sakurai, T. Matuda and M. Hiraoka, Dechlorination and destruction of PCDD, PCDF and PCB on selected fly ash from municipal waste incineration, *Chemosphere*, 2002, **46**, 1255–1262.
46 W. Wu, J. Xu, H. Zhao, Q. Zhang and S. Liao, A practical approach to the degradation of polychlorinated biphenyls in transformer oil, *Chemosphere*, 2005, **60**, 944–950.
47 G. M. Khan, G. Y. Kim, T. S. Akinrelere and S. H. Moon, Electroenzymatic mineralization of 2-chlorobiphenyl in synthetic wastewater, *Desalination*, 2007, **211**, 212–221.
48 P. Kaštánek, K. Demnerová and Y. Ma, Decontamination of wastewater contaminated by polychlorinated biphenyls (PCBs), *Water Sci. Technol.*, 2004, **50**, 131–138.
49 H. Nollet, M. Roels, L. Lutgen, P. V. D. Meeren and W. Verstraete, Removal of PCBs from wastewater using fly ash, *Chemosphere*, 2003, **53**, 655–665.
50 J. H. Carey, J. Lawrence and H. M. Tosine, Photodechlorination of PCB's in the presence of titanium dioxide in aqueous suspensions, *Bull. Environ. Contam. Toxicol.*, 1976, **16**, 697–701.
51 A. S. Westover, A. K. Kercher, M. Kornbluth, M. Naguib, M. J. Palmer, D. A. Cullen and N. J. Dudney, Plasma Synthesis of Spherical Crystalline and Amorphous Electrolyte Nanopowders for Solid-State Batteries, *ACS Appl. Mater. Interfaces*, 2020, **12**, 11570–11578.
52 H. Asadzadeh Patehkhor, M. Fattahi and M. Khosravi-Nikou, Synthesis and characterization of ternary chitosan–TiO_2–ZnO over graphene for photocatalytic degradation of tetracycline from pharmaceutical wastewater, *Sci. Rep.*, 2021, **11**, 1–17.
53 K. Nagao, A. Hayashi and M. Tatsumisago, Mechanochemical synthesis and crystallization of Li_3BO_3-Li_2CO_3 glass electrolytes, *J. Ceram. Soc. Jpn.*, 2016, **124**, 915–919.
54 N. M. Mahmood, M. Ghezelbash, M. Shabanian, F. Aryanasab and M. R. Saeb, Efficient removal of cationic dyes from colored wastewaters by dithiocarbamate-functionalized graphene oxide nanosheets: From synthesis to detailed kinetics studies, *J. Taiwan Inst. Chem. Eng.*, 2017, **81**, 239–246.
55 B. Yang, S. Wang, G. Yu and Y. Zhou, Electrocatalytic reduction of 2-chlorobiphenyl in contaminated water using palladium-modified electrode, *Sep. Purif. Technol.*, 2008, **63**, 353–359.
56 C. S. Hong, Y. Wang and B. Bush, Kinetics and products of the TiO_2 photocatalytic degradation of 2-chlorobiphenyl in water, *Chemosphere*, 1998, **36**, 1653–1667.
57 I. W. Huang, C. S. Hong and B. Bush, Photocatalytic degradation of PCBs in TiO_2 aqueous suspensions, *Chemosphere*, 1996, **32**, 1869–1881.
58 P. Zhang, R. J. Scrudato, J. J. Pagano and R. N. Roberts, Photodecomposition of PCBs in aqueous systems using TiO_2 as catalyst, *Chemosphere*, 1993, **26**, 1213–1223.
59 M. A. Yusoff, S. S. Imam, I. Shah and R. Adnan, Photocatalytic activity of bismuth oxyiodide nanospheres and nanoplates, *Mater. Res. Express*, 2019, **6**, 0850g5.
60 F. S. Tehrani, H. Ahmadian and M. Aliannezhadi, Hydrothermal synthesis and characterization of WO_3 nanostructures: Effect of reaction time, *Mater. Res. Express*, 2020, **7**, 015911.
61 R. Lei, H. Zhang, H. Ni, R. Chen, H. Gu and B. Zhang, Novel ZnO nanoparticles modified WO3 nanosheet arrays for enhanced photocatalytic properties under solar light illumination, *Appl. Surf. Sci.*, 2019, **463**, 363–373.
62 Z. Qu, Y. Su, L. Sun, F. Liang and G. Zhang, Study of the structure, electronic and optical properties of BiOI/Rutile-TiO_2 heterojunction by the first-principle calculation, *Materials*, 2020, **13**, 323.
63 P. J. Boruah, R. R. Khanikar and H. Bailung, Synthesis and Characterization of Oxygen Vacancy Induced Narrow Bandgap Tungsten Oxide ($WO_3 - x$) Nanoparticles by Plasma Discharge in Liquid and Its Photocatalytic Activity, *Plasma Chem. Plasma Process.*, 2020, **40**, 1019–1036.
64 A. Gnanaprakasam, V. M. Sivakumar and M. Thirumarimurugan, Influencing Parameters in the Photocatalytic Degradation of Organic Effluent *via* Nanometal Oxide Catalyst: A Review, *Indian J. Eng. Mater. Sci.*, 2015, **2015**, 1–16.
65 X. X. Fan, T. Yu, L. Z. Zhang, X. Y. Chen and Z. G. Zou, Photocatalytic degradation of acetaldehyde on mesoporous TiO_2: Effects of surface area and crystallinity on the photocatalytic activity, *Chin. J. Chem. Phys.*, 2007, **20**, 733–738.
66 N. M. Flores, U. Pal, R. Galeazzia and A. Sandoval, Effects of morphology, surface area, and defect content on the photocatalytic dye degradation performance of ZnO nanostructures, *RSC Adv.*, 2014, **4**, 41099–41110.
67 H. F. Moafi, M. A. Zanjanchi and A. F. Shojaie, Tungsten-doped ZnO nanocomposite: Synthesis, characterization, and highly active photocatalyst toward dye photodegradation, *Mater. Chem. Phys.*, 2013, **139**, 856–864.
68 O. Mekasuwandumrong, P. Pawinrat, P. Praserthdam and J. Panpranot, Effects of synthesis conditions and annealing post-treatment on the photocatalytic activities of ZnO nanoparticles in the degradation of methylene blue dye, *Chem. Eng. J.*, 2010, **164**, 77–84.

69 S. Ameen, H. Seo, M. S. Akhtar and H. Shik, Novel graphene/polyaniline nanocomposites and its photocatalytic activity toward the degradation of rose Bengal dye, *Chem. Eng. J.*, 2012, **210**, 220–228.

70 B. Hayati, N. M. Mahmoodi, M. Arami and F. Mazaheri, Dye Removal from Colored Textile Wastewater by Poly(propylene imine) Dendrimer: Operational Parameters and Isotherm Studies, *Clean: Soil, Air, Water*, 2011, **39**, 673–679.

71 J. Jiang, H. Wang, X. Chen, S. Li, T. Xie, D. Wang and Y. Lin, Enhanced photocatalytic degradation of phenol and photogenerated charges transfer property over BiOI-loaded ZnO composites, *J. Colloid Interface Sci.*, 2017, **494**, 130–138.

72 J. Wen, J. Xie, X. Chen and X. Li, A review on g-C3N4 -based photocatalysts, *Appl. Surf. Sci.*, 2017, **391**, 72–123.

73 N. Natkritta, D. Channei, B. Inceesungvorn and C. Zhao, Visible Light-Driven BiOI/ZnO Photocatalyst Films and Its Photodegradation of Methoxyl Insecticide, *Int. J. Appl. Sci. Technol.*, 2018, **11**, 297–304.

74 W. Zhang, H. Fei, N. Wang, D. Li, Q. Chen, H. Xu, H. Li, J. He and J. Lu, p–n Heterojunction of BiOI/ZnO nanorod arrays for piezo-photocatalytic degradation of bisphenol A in water, *J. Hazard. Mater.*, 2020, **399**, 123109.

75 H. J. Yoon, Y. I. Choi, E. S. Jang and Y. Sohn, Graphene, charcoal, ZnO, and ZnS/BiOX (X = Cl, Br, and I) hybrid microspheres for photocatalytic simulated real mixed dye treatments, *J. Ind. Eng. Chem.*, 2015, **32**, 137–152.

76 N. M. Mahmoodi, M. Ghezelbash, M. Shabanian, F. Aryanasab and M. R. Saeb, Efficient removal of cationic dyes from colored wastewaters by dithiocarbamate-functionalized graphene oxide nanosheets: From synthesis to detailed kinetics studies, *J. Taiwan Inst. Chem. Eng.*, 2017, **81**, 239–246.

77 M. Khatamian, A. A. Khandar, B. Divband, M. Haghighi and S. Ebrahimiasl, Heterogeneous photocatalytic degradation of 4-nitrophenol in aqueous suspension by Ln (La^{3+}, Nd^{3+} or Sm^{3+}) doped ZnO nanoparticles, *J. Mol. Catal. A: Chem.*, 2012, **365**, 120–127.

78 O. Bechambi, S. Sayadi and W. Najjar, Photocatalytic degradation of bisphenol A in the presence of C-doped ZnO: Effect of operational parameters and photodegradation mechanism, *J. Ind. Eng. Chem.*, 2015, **32**, 201–210.

79 S. M. Lam, J. C. Sin, A. Z. Abdullah and A. R. Mohamed, Sunlight responsive WO_3/ZnO nanorods for photocatalytic degradation and mineralization of chlorinated phenoxyacetic acid herbicides in water, *J. Colloid Interface Sci.*, 2015, **450**, 34–44.

80 T. T. T. Nguyen, T. N. Nguyen, Q. V. Tran, H. K. Nguyen, M. T. Nguyen and T. H. N. Le, Synthesis, characterisation, and effect of pH on degradation of dyes of copper-doped TiO_2, *J. Exp. Nanosci.*, 2016, **11**, 226–238.